JACS
JOURNAL OF THE AMERICAN CHEMICAL SOCIETY

Article

pubs.acs.org/JACS

Metal and Metal Oxide Interactions and Their Catalytic Consequences for Oxygen Reduction Reaction

Qingying Jia,[†] Shraboni Ghoshal,[†] Jingkun Li,[†] Wentao Liang,[‡] Guangnan Meng,[§] Haiying Che,[∥] Shiming Zhang,[∥] Zi-Feng Ma,*[,∥] and Sanjeev Mukerjee*[,†]

[†]Department of Chemistry, Chemical Biology and [‡]Department of BiologyNortheastern University, Boston, Massachusetts 02115 United States

[§]ULVAC Technologies, Inc., 401 Griffin Brook Drive, Methuen, Massachusetts 01844, United States

[∥]Shanghai Electrochemical Energy Devices Research Center, Department of Chemical Engineering, Shanghai Jiao Tong University, Shanghai 200240, People's Republic of China

Supporting Information

ABSTRACT: Many industrial catalysts are composed of metal particles supported on metal oxides (MMO). It is known that the catalytic activity of MMO materials is governed by metal and metal oxide interactions (MMOI), but how to optimize MMO systems via manipulation of MMOI remains unclear, due primarily to the ambiguous nature of MMOI. Herein, we develop a Pt/NbO_x/C system with tunable structural and electronic properties via a modified arc plasma deposition method. We unravel the nature of MMOI by characterizing this system under reactive conditions utilizing combined electrochemical, microscopy, and in situ spectroscopy. We show that Pt interacts with the Nb in unsaturated NbO_x owing to the oxygen deficiency in the MMO interface, whereas Pt interacts with the O in nearly saturated NbO_x, and further interacts with Nb when the oxygen atoms penetrate into the Pt cluster at elevated potentials. While the Pt−Nb interactions do not benefit the inherent activity of Pt toward oxygen reduction reaction (ORR), the Pt−O interactions improve the ORR activity by shortening the Pt−Pt bond distance. Pt donates electrons to NbO_x in both Pt−Nb and Pt−O cases. The resultant electron eficiency stabilizes low-coordinated Pt sites, hereby stabilizing small Pt particles. This determines the two characteristic features of MMO systems: dispersion of small metal particles and high catalytic durability. These findings contribute to our understandings of MMO catalytic systems.

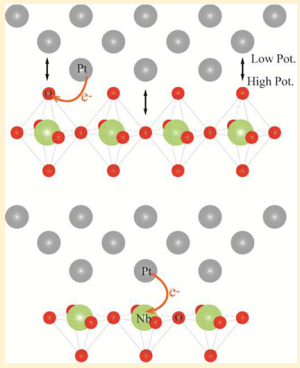

INTRODUCTION

Metal particles supported on metal oxides (MMO) are among the most important catalytic systems in heterogeneous catalysis with versatile applications such as petroleum refinement, energy conversion, and hydrogenation.[1−5] The broad applications of this system arise largely from strong metal−support interactions (SMSI), which can not only facilitate dispersion of small particles hereby promoting utilization of costly metal, but also favorably alter the catalytic properties of supported metal particles toward many reactive processes.[4−6] Despite recent progress in developing MMO systems for catalytic applications, some of the most fundamental aspects of SMSI including the type of the interfacial bonds and the associated direction of electron transfer across MMO interfaces remain unclear. It is generally believed that SMSI arises from the d-orbital overlap between the metal atom and the reduced cation of the oxide (i.e., metal−metal interactions);[2,3,5,7,8] whereas metal−oxygen interactions were also reported for various MMO systems composed of either reducible[9−11] or irreducible oxides.[12−14] For each proposed SMSI type, electron donation from metal to oxide,[8,14,15] from oxide to metal,[2,7,16] or insignificant electron transfer[17,18] has been reported, even on the same MMO system. Taking platinum clusters supported on zeolite Y as an example of the MMO system with irreducible oxide support, Dalla Betta et al.[15] observed electron-deficient Pt clusters and proposed partial electron transfer from Pt to zeolite. Gallezot et al.[19] however argued that the electron-deficient nature of Pt is an intrinsic property of small particles rather than caused by electron transfer. On the contrary, Barthomeuf et al.[20] claimed an electron-enriched configuration of Pt due to the electron transfer from Y zeolite to Pt. Later, Ponec's[21] and Koningsberger's[22] groups stated that there is no significant electron transfer in this MMO system. Similar debates also exist on the MMO system with reducible oxide support. For example, Mitlin and co-workers[10,23] systematically studied the Pt/NbO_x system and claimed that electronic charge flows from NbO_x to Pt for x = 0, 1, 2, and the flow direction is reversed for Pt/Nb_2O_5. They further pointed out that Pt interacts with the oxygen rather than Nb in all cases, which contradicts the common view of metal−metal interactions in MMO systems with reducible oxide supports.[2,3,5,7] In contrast, Sasaki et al.[18] stated that there is no electronic interference between Pt and Nb_2O_5; and NbO_2 either donate or share d-electrons with Pt.

Received: March 13, 2017
Published: May 23, 2017

DOI: 10.1021/jacs.7b02378
J. Am. Chem. Soc. 2017, 139, 7893−7903

These conflicting results preclude rational design of MMO systems through manipulating metal and metal oxide interactions (denoted as MMOI here to account for both metal−metal and metal−oxygen interactions).

Elucidating the nature of MMOI poses a substantial challenge because of the difficulties in characterizing MMO interfaces under relevant reaction conditions. The MMO interface by its very nature is generally buried underneath the metal particles. This configuration with the associated screening effects[7] severely impedes direct microscopic observation as well as bulk spectroscopic probing. Such difficulties obstruct efforts to establish the relationships between MMOI and catalytic properties, especially for MMO systems with large metal particles. Additional difficulties arise from the high temperature treatment of the MMO system under H_2 atmosphere to activate SMSI.[2,5] This treatment usually causes the migration of oxides onto metal surfaces,[7,24] and/or the alloying between the supported metal clusters and the metal in the oxides.[25,26] Consequently, the MMOI may come from the underlying oxides, the oxide overlayers, and/or the alloying phases. This rules out a clear-cut identification of the observed interactions, which is made even worse by the fact that it is unclear whether the MMOI with oxide overlayers or underlayers have the same nature.[7]

Herein, we aim to unravel the nature of interfacial MMOI and its catalytic consequences. To pursue this, we probe MMOI on representative Pt/NbO_x/C systems prepared by a modified coaxial cathodic arc plasma deposition (APD) sputtering method. This method allows for sample preparation under mild conditions with some controls over the stoichiometry, particle size, and interfacial structure of the final products. Nb_2O_5 is chosen here as it exhibits the highest reducibility and hence the strongest SMSI behavior among regular transition metal oxides.[2] Meanwhile, the high negative reduction potential of Nb prevents its alloying with Pt. Indeed, a Pt−Nb alloy has never been achieved until recently by us as part of this work (denoted as A-PtNb, which is presented here as a reference catalyst exemplifying the Pt−Nb alloying phase. Detailed synthesis and characterizations of A-PtNb will be reported elsewhere). Moreover, NbO_x ($x \geq 2$) is stable under highly corrosive and acidic conditions such as fuel cell electrodes.[4] This is essential for many catalytic applications, and also enables in situ probing of MMOI under electrochemical environments. We use in situ X-ray absorption spectroscopy (XAS) together with complementary techniques including X-ray diffraction (XRD), transmission electron microscopy (TEM), and X-ray photoelectron spectroscopy (XPS) to investigate the nature of MMOI in Pt/NbO_x/C systems with tunable interface morphologies. The results provide firm evidence for the nature of MMOI under reactive conditions, and reveal the oscillating nature of MMOI not previously recognized. The unraveled nature of MMOI in the Pt/NbO_x/C system is explicitly correlated to their catalytic activity and durability toward oxygen reduction reaction (ORR) in acidic media.

EXPERIMENTAL METHODS

Catalysts Synthesis via Arc Plasma Deposition Method. Commercial Pt, Nb_2O_5, and/or Nb powders (Toshima Materials) were deposited onto carbon substrate in a stirring vessel under a vacuum of ~10^{-6} Torr and mild temperature (≤350 °C) by a commercial coaxial cathodic APD system (ULVAC Technologies, Inc.) (Scheme S1). Detailed deposition processes are given in Supporting Information (Table S1). The system was slightly modified by adding a ceramic heater underneath the stirring vessel, in order to control the sample temperature. We also installed a third APD source to increase the flexibility of deposition modes. A K-type thermocouple was used to monitor the sample temperature during the process. The coating process includes the following steps:

(1) Prior to use, moisture was removed from carbon powder surface by leaving carbon powder in an oven at 200 °C for 2 h.

(2) The dry carbon powder (usually about 15 mL) were loaded into the vessel, then we started depressurize the vacuum chamber. The valve was opened very slowly to avoid any disturbance of the carbon nanoparticles. The vessel started to rotate at a slow speed (9 rpm), in order to mix the carbon powder homogeneously in the vessel. In the meanwhile, the heater warmed up gradually. It usually took about an hour to reach the base temperature, 350 °C, and vacuum of 10^{-4} Pa.

(3) As the base condition was reached, the deposition started by igniting the APD sources on the selected targets. The stirring speed increased up to about 30−40 rpm during the deposition. We regularly inspected the stirring condition through the chamber window, and monitored the sample temperature and chamber pressure. We waited about 5 min between the depositions of two layers.

(4) After the deposition was complete, we reduced the heater power and allowed the sample to cool down slowly. We kept stirring the powder and pumping down the chamber during the cooling down. It took about 1 h for the chamber to cool from 350 to 150 °C. Then we stopped the stirring and shut off vacuum system. We let the chamber and sample to cool down to room temperature overnight, under base pressure about 1−10 Pa in the chamber.

(5) The chamber was vented with N_2 or Ar very slowly, for the same reason to avoid the disturbance to the carbon nanoparticles. It usually took about 30 min to reach the atmosphere pressure from 10 Pa. Then the final product was collected and sealed into glass vials.

The synthesis of A-PtNb is given in the Supporting Information.

Ex Situ Physicochemical Characterizations. Transmission electron microscopy TEM) was conducted on a JEOL 2010 field emission gun (FEG) with an acceleration voltage of 200 kV with samples deposited on a holey carbon film on a 300 mesh copper grid. X−ray diffraction experiments were conducted via a Bragg−Brentano para-focusing UltimaIV powder diffractometer utilizing a Cu K_α radiation source from Rigaku. Unit cell constants of the samples were refined with PDXL software program provided by Rigaku Corporation. Sample composition was determined by the X-ray fluorescence. Particle morphology and Fe, C, and emental mapping were performed on a Hitachi S-4800 field emission scanning electron microscope (SEM) equipped with energy dispersive X-ray spectroscopy (EDX) with an accelerating voltage of 3−5 keV. Samples were mounted on a carbon-free adhesive stub attached to an aluminum sample stage. Raman spectra were collected using a Thermo Scientific DXR2xi Raman microscope.

In Situ XAS Experiments. The ink for the XAS electrode was composed of 8.2 MΩ purity deionized water (Millipore), 2-propanol (HPLC grade, Aldrich), 5 wt % Nafion solution (Aldrich), and the catalyst powder. The ink was sprayed onto a Zoltek carbon cloth on a piece glass heated on 40 °C. The final Pt and Nb geometric loadings were chosen to give 0.1 transmission spectra edge heights at the Pt L_3 and Nb K edges, respectively. The XAS experiments were conducted at room temperature in a previously described in situ spectro-electrochemical half−cell[27] in which continuously purged (N_2 or O_2) 0.1 M $HClO_4$ was circulated. The samples were conditioned in 0.1 M $HClO_4$ under vacuum for 40 min to remove surface oxides and contaminants before transferred into the cell. Potentiostatic control was maintained with an Autolab PGSTAT30 potentiostat (Metrohm USA, formerly Brinkman Instruments). The voltage cycling limits were 0.05 to 1.1 V. All data were collected in the fluorescence mode at the beamlines of X3B and X19A at the National Synchrotron Light Source (NSLS) (Brookhaven National Laboratory, NY); and the beamline of 2-2 at the SSRL, Stanford Linear Accelerator Center. Typical experimental procedures were utilized with details provided in our previous work.[28] The data were processed and fitted using the Ifeffit−based Athena[29] and Artemis[30] programs. Scans were calibrated, aligned and

DOI: 10.1021/jacs.7b02378
J. Am. Chem. Soc. 2017, 139, 7893−7903

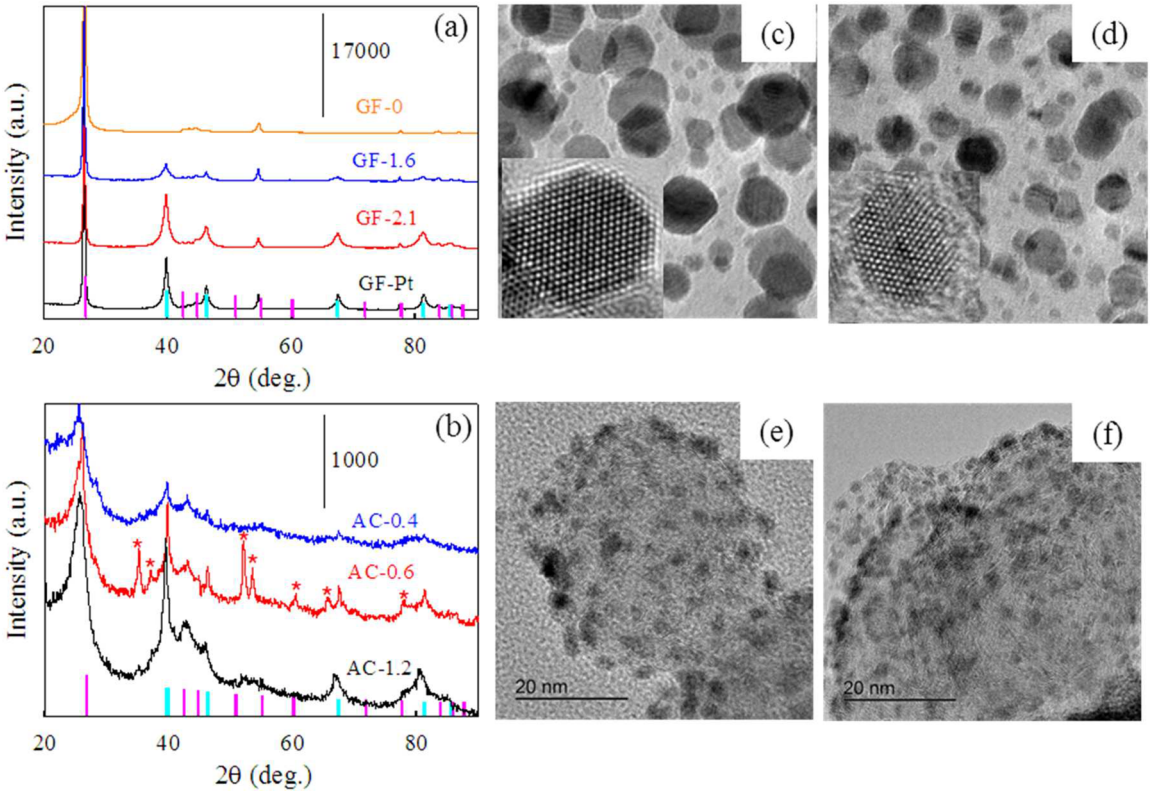

Figure 1. XRD patterns of GF-supported (a) and AC-supported (b) samples. Note the dramatic difference in the XRD peak intensity between GF- and AC- supported samples as indicated by the intensity of the scale bars. The cyan and purple bars indicate the diffraction patterns of Pt (#9008480) and graphite (#9008569). The red stars indicate the peaks also identified in the XRD patterns of the NbO_2 standard collected at the same conditions (Figure S3b). TEM images of GF-Pt (c), GF-1.6 (d), AC-1.2 (e), and AC-0.6 (f) with the same scale. Insets of (c) and (d) display the high resolution TEM images of representative Pt particles.

normalized with background removed using the IFEFFIT suite.[31] The $\chi(R)$ were modeled using single scattering paths calculated by FEFF6.[32]

Ink Preparation for Rotating Disk Electrode (RDE), Measurement and Accelerated Stress Test (AST). The catalyst powder was added to a 5−10 mL solution, containing 20 vol % isopropanol (J.T. Baker, 99.9%), 79.6 vol % Nanopure water, and 0.4 vol % Nafion solution (Ion Power) to form a catalyst ink. The ink was further mixed under ultrasonication for a minimum of 1 h while the temperature was maintained below 50 °C. A volume of 8 μL of the mixed catalyst ink was deposited in one drop onto the 5.0 mm diameter gold tip using a micropipette, containing about 2.0−4.0 μg of Pt. The gold RDE tip remained upright and level as the shaft rotated at a speed of about 500 rpm, allowing the tip to dry overnight in air. This created a thin uniform catalyst film with an area of 0.196 cm^2 on the gold tip.

The modulated speed rotator, RDE shaft and 5.0 mm diameter gold tips (Pine Instruments, USA) and SP-150 single potentiostat/galvanostat/ZRA (BioLogic Science Instruments) were used to determine the Pt electrochemical surface area (ECSA) and area-specific and mass-specific activities toward ORR. The cyclic voltammograms (*CV*) spectra were taken for all prepared samples in Ar-saturated 0.1 M $HClO_4$ solution (GFS Chemicals Inc. OH, USA, double distilled, 70 wt % $HClO_4$) with a scan rate of 20 $mV{\cdot}s^{-1}$ and a rotation speed of 400 rpm for positive-going potential sweeps between 0.05 to 1.05 V versus the reversible hydrogen electrode (denoted as V_{RHE}). The ECSA values were derived by integrating the hydrogen desorption charges using 210 $\mu C\ cm^2$ as the specific capacitance for Pt, and the gold tip geometric surface area of 0.196 cm^2. ORR polarization curves for the prepared samples were recorded in an O_2-saturated solution with a scan rate of 20 $mV{\cdot}s^{-1}$ and a rotation speed of 1600 rpm. RDE experiments were conducted with a gold working electrode, Pt mesh counter electrode, and H_2 gas/Pt mesh RHE reference electrode in a 35 °C constant temperature three compartment glass cell. The reference electrode was separated from the working electrode by means of a closed stopcock Luggin capillary to prevent hydrogen gas from leaking into the working electrode compartment. The counter electrode was separated from the working electrode cell by means of a glass frit. The electrolyte inner IR drop was ignored in ORR activity calculation.

In general, severe platinum dissolution (Pt-stress) happens within a voltage window of 0.1−1.0 V. Therefore, a 0.1−1.0 V square wave with duration of 3 s for each voltage level has been used for Pt-stress testing. The reversible hydrogen electrode (RHE) at a constant temperature of 35 °C was used as the reference electrode. ECSAs and ORR activities were recorded at the beginning-of-life (BOL) (~200 cycles), middle-of-life (MOL) (12 500 cycles), and end-of-life (EOL) (25 000 cycles) stages.

RESULTS

Electrocatalyst Preparation and Characterization. We applied a modified APD sputtering method for sample preparation to acquire more flexibility in the deposition mode so as to gain finer control over the morphology and composition of the supported Pt/NbO_x (preparation processes are given in the Experimental Methods section). In particular, two different types of carbon, highly ordered graphene nanoflakes (denoted as GF) (Graphene Supermarket) and highly amorphous carbon powders (denoted as AC) (BASF) with distinctly different crystallinity evidenced by Raman spectroscopy (Figure S1), were used as the substrate to dictate the morphological properties of the supported Pt/NbO_x systems. As a result, two groups of samples with distinctly different morphologies were formed. The samples on GF are dominated by large (≥5 nm) and crystalline Pt particles; whereas the samples on AC are dominated by small (≤3 nm) and amorphous Pt particles as

DOI: 10.1021/jacs.7b02378
J. Am. Chem. Soc. 2017, 139, 7893−7903

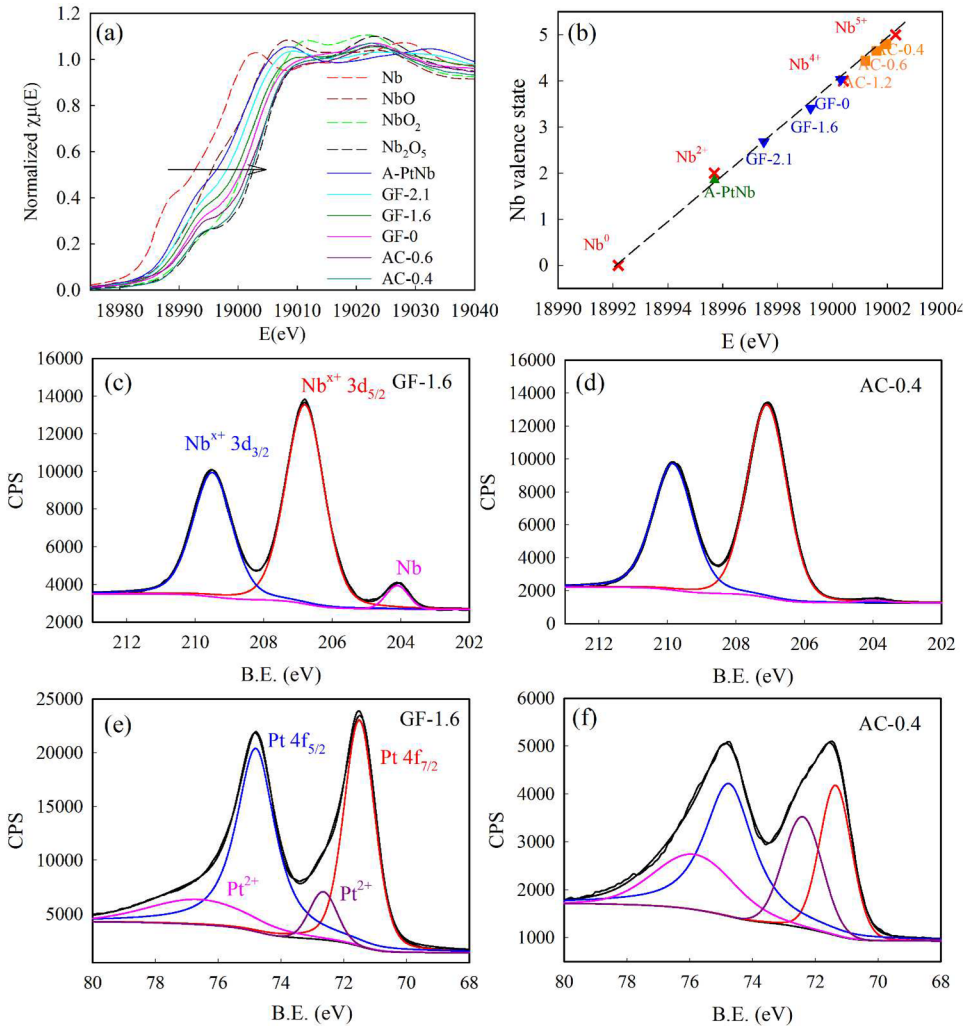

Figure 2. XANES spectra collected at the Nb K-edge for indicated samples and Nb standards (a); the Nb valence state of tested samples as a function of their E_{edge}(s); the black dashed line is a guide to the eye (b). Nb 3d (c, d) and Pt 4f XPS (e, f) spectra of GF-1.6 (left) and AC-0.4 (right). Note the big difference in the peak intensity of the Pt 4f XPS spectra between the two samples.

evidenced by the combined XRD and TEM results (Figure 1). SEM-EDX confirmed the drastically different surface morphology between the two groups of samples, and the relatively uniform distributions of the Pt, Nb, and O elements in both cases (Figure S2). Further, the structural and electronic properties of Pt/NbO_x/GF and Pt/NbO_x/AC can be fine-tuned by adjusting the Pt/Nb atomic ratio via tuning the deposition mode (a complete list of the samples prepared with varied parameters is summarized in Table S2). To facilitate the discussions, the synthesized catalysts are labeled as GF-$n_{Pt/Nb}$ or AC-$n_{Pt/Nb}$ where $n_{Pt/Nb}$ represents the Pt/Nb atomic ratio given by X-ray fluorescence.

In addition to the structural properties, the bulk average valence states of the Nb on the two carbon substrates are also markedly different. The Nb K-edge X-ray absorption near edge structure (XANES) spectra (the Nb K-edge XAS spectra do not change with the applied potential within the entire potential window from 0.1 to 1.5 V_{RHE} for all studied samples (Figure S6), and thus the merged data were used for analysis) displayed in Figure 2a indicate that the valence states of the Nb_2O_5 supported on AC remains close to +5, but is reduced to around +4 when supported on GF (Figure 2b). The valence states of Nb in the Pt/NbO_x/C systems are derived from their E_{edge}, which is defined as the energy at which the normalized absorption of XANES is precisely one-half (Figure 2a). This is justified by the nearly linear relationship between the valence state of Nb standard references (Nb foil, NbO, NbO_2, and Nb_2O_5) and their respective E_{edge} (Figure 2b). These results show that the Nb_2O_5 can be prereduced by graphitized carbon at mild conditions rather than high temperature treatment, hereby avoiding the possible formation of oxide overlayers and alloying (vide infra).

With decreasing $n_{Pt/Nb}$, the XRD peak intensities of both GF and AC supported Pt clusters decrease (Figure 1a and b); and the crystallite size of GF-supported Pt clusters decreases (Table S3), which is accompanied by the decreasing particle size estimated by TEM (Figure 1c and d). Concomitantly, the valence state of the Nb within the GF or AC supported samples increases monotonically with decreasing $n_{Pt/Nb}$ (Figure 2b). These results show that it is possible to control the particle size of Pt and the valence state of Nb in the Pt/NbO_x/C catalysts.

XPS verifies the presence of Pt and Nb in the representative Pt/NbO_x/C catalysts (Figure 2). The Pt 4f XPS spectra (Figure 2e and f) indicate that the Pt in GF-1.6 is mainly in the metallic state, whereas a significant portion of the Pt in AC-0.4 is in the oxidized state. The Nb 3d XPS spectra (Figure 2c and d) confirm that vast majority of the Nb in the Pt/NbO_x/C catalysts

DOI: 10.1021/jacs.7b02378
J. Am. Chem. Soc. 2017, 139, 7893−7903

Table 1. Summaries of EXAFS Fitting Results of Indicated Samples at Various Applied Potetnials vs RHE in O_2-Saturated 0.1 M $HClO_4$ Electrolyte[a]

		Pt−Pt scattering			Pt−Nb scattering			Pt−O scattering			E_0 (eV)
potential vs RHE	catalyst symbol	R (Å)	CN	σ^2 (Å^2)	R (Å)	CN	σ^2 (Å^2)	R (Å)	CN	σ^2 (Å^2)	
0.10 V	GF-1.6	2.75(1)	7.3(5)	0.005(1)	2.75(2)	0.9(4)	0.005(1)				6.7(5)
	AC-0.6	2.73(1)	7.0(1.1)	0.007(1)	2.72(4)	0.7(4)	0.007(1)	1.99(4)	0.5(2)	0.01(f)	6.0(1.0)
	AC-0.4	2.73(1)	4.9(4)	0.007(1)	2.76(3)	0.4(3)	0.008(1)	1.97(1)	0.8(3)	0.010(7)	5.9(8)
0.54 V	GF-Pt	2.76(1)	9.7(7)	0.005(1)	–	–	–	–	–	–	7.9(6)
	GF-2.1	2.76(1)	8.1(6)	0.007(f)	2.76(1)	0.5(2)	0.007(f)				7.3 (8)
	GF-1.6	2.75(1)	7.5(6)	0.006(1)	2.75(2)	0.8(2)	0.006(1)				6.6(5)
	AC-0.6	2.73(1)	7.1(8)	0.008(1)	2.75(5)	0.9(3)	0.008(1)	1.99(3)	0.7(5)	0.01(f)	6.3(1.0)
	AC-0.4	2.74(2)	4.2(9)	0.007(2)	2.76(4)	1.0(4)	0.007(2)	1.97(2)	1.3(5)	0.009(6)	6.1(2.0)
	A-PtNb	2.77(1)	8.1(7)	0.005(1)	2.79(1)	2.3(3)	0.005(1)				7.2(5)
0.90 V	GF-1.6	2.75(1)	7.2(6)	0.005(1)	2.76(2)	0.8(2)	0.005(1)				7.0(6)
	AC-0.6	2.73(1)	7.5(1.0)	0.009(1)	2.77(8)	0.5(6)	0.009(1)	1.99(2)	0.9(2)	0.01(f)	6.1(1.2)
	AC-0.4	2.73(3)	4.9(1.2)	0.010(3)	2.77(7)	0.9(7)	0.010(3)	1.97(2)	1.4(5)	0.010(6)	5.8(2.3)
1.10 V	GF-2.1	2.75(1)	6.8(1.1)	0.007(1)	2.76(4)	0.4(4)	0.007(1)	2.01(4)	0.4(1)	0.01(f)	6.1(1.4)
	GF-1.6	2.75(1)	6.6(1.1)	0.005(1)	2.75(2)	1.3(3)	0.005(1)	1.98(4)	0.6(3)	0.01(f)	6.4(1.1)
	AC-0.4	2.73(1)	4.9(8)	0.010(f)	2.77(3)	1.2(7)	0.010(f)	1.98(1)	1.7(6)	0.008(6)	5.9(9)

[a]The numbers in the parentheses represent the uncertainties from the EXAFS fittings. S_0^2 values were fixed at 0.80 and 0.76 for Pt and Nb, respectively, as obtained by fitting the reference foils. Fits were done in R-space, $k^{1,2,3}$ weighting. $1.3 < R < 3.1$ Å and $\Delta k = 2.73–12.63$ Å^{-1} were used for fitting the Pt L_3-edge data.

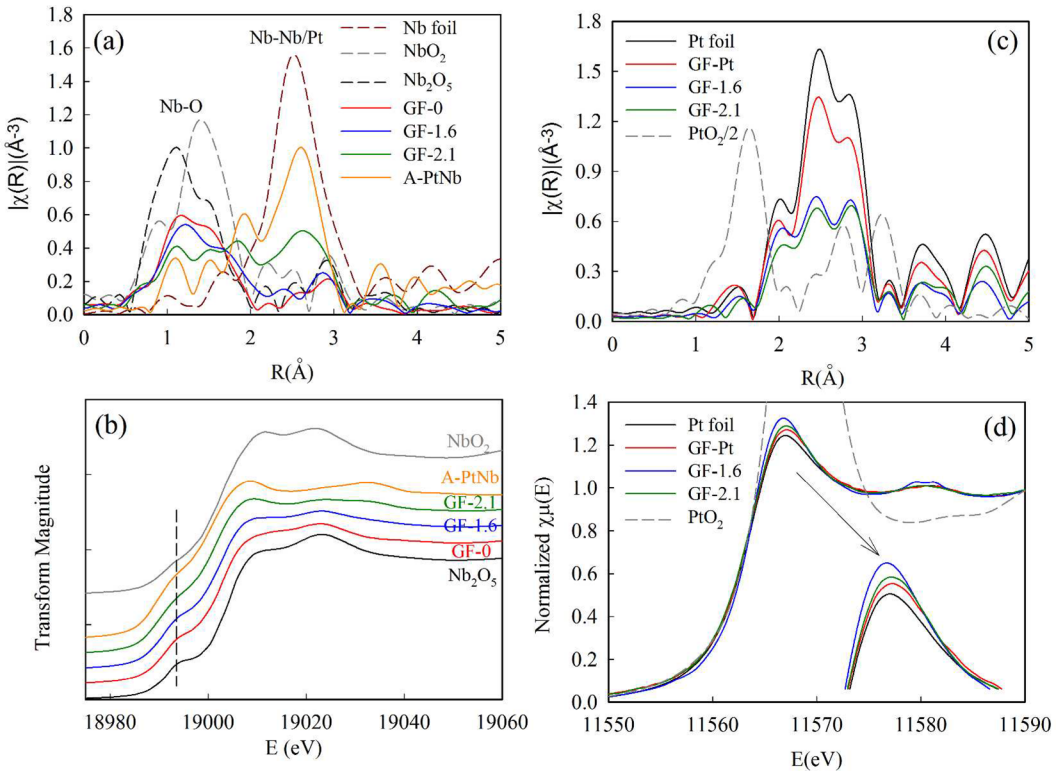

Figure 3. FT-EXAFS (a) and XANES (b) spectra collected at the Nb K-edge for GF-supported samples and Nb standards; FT-EXAFS (c) and XANES (d) spectra collected at the Pt L_3-edge for GF-supported samples at 0.54 V_{RHE} and Pt standards. The gray dashed line in (b) is a guide to the eye highlighting the intensity of the pre-edge peaks around 18993 eV.

is in the oxidized state, whereas some Nb in the A-PtNb is in the metallic state associated with the Pt−Nb alloying phase (Figure S4). This is further confirmed by XRD. The Pt−Nb alloying phase was not observed for all the Pt/NbO_x/C samples given that their lattice constants (3.925 Å) are close to that of the counterpart Pt/C (3.928 Å), whereas the A-PtNb formed upon high temperature treatment exhibits a larger lattice constant (3.942 Å) as per the Vegard's law (Table S3).[33] The codeposition of metallic Nb using a third APD source also did not lead to the formation of Pt−Nb alloying phase, but rather some NbO_2 as reflected by the XRD features (AC-0.6 in Figure 2b). These results indicate that the Pt−Nb alloying is indeed impeded by the high negative reduction potential of Nb, and is not formed at mild temperatures. In addition, the oxide overlayers were not detected by TEM for all the samples; whereas they can be readily observed by TEM for MMO

DOI: 10.1021/jacs.7b02378
J. Am. Chem. Soc. 2017, 139, 7893−7903

systems containing oxide overlayers.[24,34] The absence of oxide overlayers is further corroborated by electrochemical characterizations shown later in the electrochemical section. Overall, the two different Pt/NbO_x/C systems with tunable properties and absence of alloying phase and oxide overlayers achieved by our preparation method fulfill the prerequisites for interfacial MMOI exploration.

Pt−Nb Interactions. As indicated by the XRD and TEM results, direct deposition of Pt onto highly crystalline GF (denoted as GF-Pt) forms large and crystalline Pt particles; whereas the Nb_2O_5 deposited on GF remains amorphous (Figures 1 and S5). It is therefore not surprising to see that the particle size and crystallinity of the Pt particles formed upon codeposition with Nb_2O_5 on GF decrease with decreasing $n_{Pt/Nb}$ (Figure 1), which is further supported by the lower coordination number (CN) of Pt as obtained by extended X-ray absorption fine structure (EXAFS) fittings (Table 1) since the CN of small particles decreases with particle size.[35,36] This trend indicates that the Pt supported on amorphous NbO_x tends to form small and amorphous NPs, as widely observed on MMO systems.[5]

With increasing $n_{Pt/Nb}$, the valence state of the Nb in Pt/NbO_x/GF samples decreases and reaches +2 for the A-PtNb (Figure 2b). This trend is accompanied by the increase of the intensity of the FT-EXAFS peak of the Nb K-edge at ~2.5 Å (Figure 3a). The EXAFS fitting results on A-PtNb show that this peak arises predominately from the Nb−Pt scattering (Figure S8). The observed Nb−Pt scattering in association with the reduced Nb valence state strongly suggest the Pt−Nb interactions in the Pt/NbO_x/GF system with electron donation from Pt to Nb. The d-electron configuration rearrangements from both Nb and Pt perspective as a consequence of this electron transfer direction are confirmed by their XANES spectra. The electron-deficient configuration of Pt is indicated by the higher Pt white line intensity of Pt/NbO_x/GF compared to that of GF-Pt (Figure 3d), as the white line arises from the electron transition from the 2p orbital to the vacant 5d orbital and its intensity increases with increasing 5d vacancy.[37] Meanwhile, the enriched d-electrons in Nb are reflected by the reduced intensity of the pre-edge peak around 18993 eV that arises from the 1s−4d electron transition and decreases with increasing d-electrons (Figure 3b).[18,38] This electron transfer direction is essentially driven by the electron donation tendency from Pt with paired d-electrons to Nb cations with rather empty d-orbitals.[39]

The Pt−Nb interactions are also discernible from the Pt perspective. The FT-EXAFS peak of Pt/GF closely resembles that of the Pt reference foil (Figure 3c), and can be well fitted with a pure Pt model (Figure S7a). The codeposition of Nb_2O_5 drastically changes its shape and reduces its intensity (Figure 3c), and a Pt−Nb path must be included into the model to obtain a reasonable fit (Figure S7b). Despite the Pt−Nb interactions, the bulk average Pt−Pt bond distance (R_{PtPt} = 2.75 Å) in Pt/NbO_x/GF is identical to that of GF-Pt but shorter than that of the A-PtNb (2.77 Å) (Table 1). This agrees well with their lattice constants given by XRD, further confirming the absence of the Pt−Nb alloying phase in Pt/NbO_x/GF. These results together give firm evidence for the interfacial Pt−Nb interactions in the Pt/NbO_x/GF system with electron donation from Pt to Nb.

Pt−O Interactions. The MMOI in the Pt/NbO_x/AC system is distinctly different from that in Pt/NbO_x/GF. The FT-EXAFS spectra at the Nb K-edge of Pt/NbO_x/AC contain a prominent Nb−O scattering peak around 1.5 Å (without phase corrections); whereas the Nb−Pt scattering peaks are conspicuously absent (Figure 4a). This suggests the absence

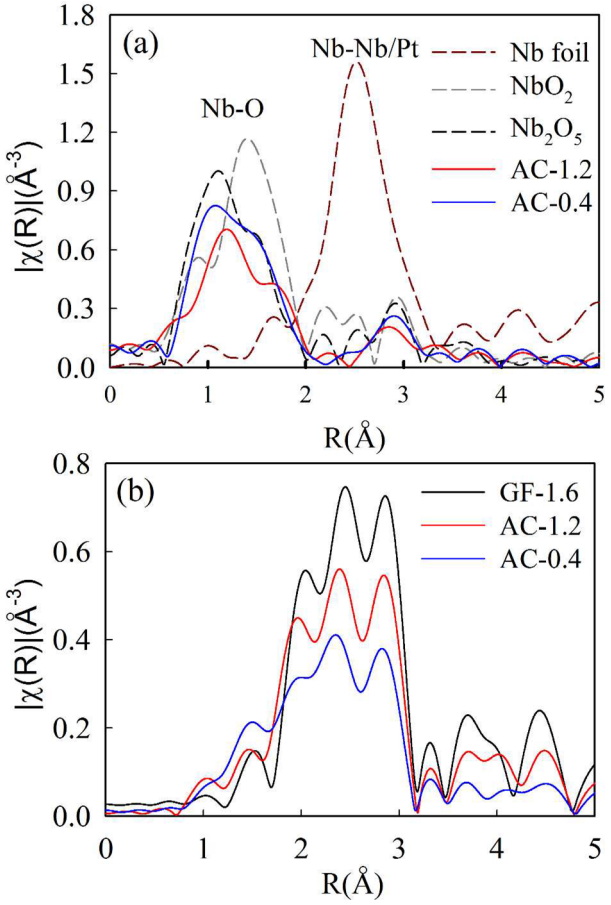

Figure 4. FT-EXAFS spectra collected at the Nb K-edge (a) and Pt L_3-edge (b) for indicated catalysts at 0.54 V_{RHE}, together with spectra of Nb standards collected ex situ.

of Nb−Pt interactions seen from the Nb perspective. From the Pt perspective, the FT-EXAFS peak intensities of the Pt/NbO_x/AC system are much lower than those of Pt/NbO_x/GF, especially those beyond 3 Å associated with long-range scattering that are very sensitive to the particle size and crystallinity (Figure 4b). Accordingly, the EXAFS fittings generally give smaller *CN* of Pt and higher Debye−Waller factor (Table S2), suggesting smaller and more disordered Pt particles in the Pt/NbO_x/AC system as also observed by XRD and TEM. The combined XAS, XRD, and TEM results indicate that the catalyst synthesized with a low $n_{Pt/Nb}$ ratio of 0.4 under low temperature (100 °C) (denoted as AC-0.4) contains the smallest Pt particles among all the Pt/NbO_x/C catalysts prepared in this work. AC-0.4 is therefore chosen for MMOI characterizations representing Pt/NbO_x/AC catalysts since small and amorphous Pt particles with a high fraction of Pt in the MMO interface greatly facilitates MMOI characterizations, plus the MMOI effect exponentially increases with decreasing metallic particle size.[40]

The FT-EXAFS of AC-0.4 collected at the Pt L_3-edge at 0.10 V_{RHE} can be well fitted without including a Pt−Nb scattering path in the model (Figure 5a), and even if the Pt−Nb path was included an insignificant CN_{PtNb} of 0.4 ± 0.3 was obtained. Meanwhile, a Pt−O path must be included in order to fit the FT-EXAFS peak around 1.5 Å (Figure 5a), associated with a

DOI: 10.1021/jacs.7b02378
J. Am. Chem. Soc. 2017, 139, 7893−7903

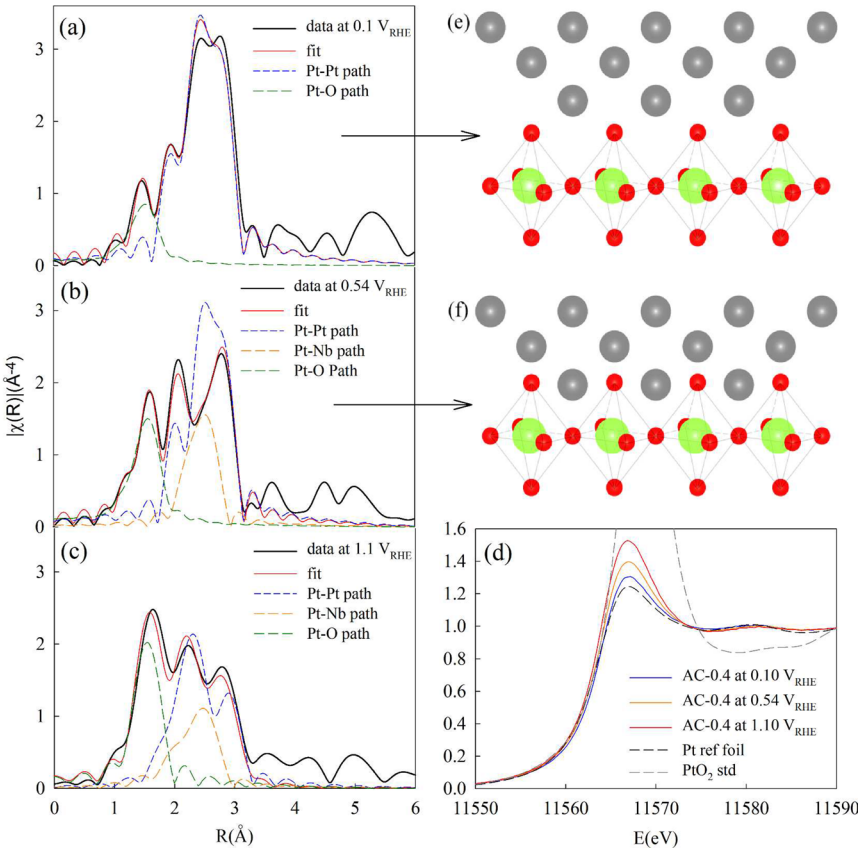

Figure 5. In situ FT-EXAFS data of AC-0.4 collected at the Pt L_3-edge at 0.1 V_{RHE} (a), 0.54 V_{RHE} (b), and 1.1 V_{RHE} (c) in an O_2-saturated 0.1 M $HClO_4$ electrolyte together with the first shell EXAFS fitting results. The corresponding XANES spectra are shown in (d). The interfacial MMO structures derived from the results presented in (a) and (b) are illustrated in (e) and (f), respectively. Silver, green, and red balls represent Pt, Nb, and O, respectively.

non-negligible CN_{PtO} of 0.8 ± 0.3. The Pt−O interactions are further reflected by the much higher Pt white line intensity compared to the Pt foil (Figure 5d), which indicates the pronounced electron transfer from Pt to O. This agrees well with the XPS result of a high fraction of Pt in AC-0.4 being in the oxidized state (Figure 2f). The oxygen species bound to Pt is unlikely from water dissociation since the spectrum was collected at 0.1 V_{RHE} in a N_2-sataurated 0.1 $HClO_4$ electrolyte, under which the Pt surface is negatively charged and covered by the underpotential deposited hydrogen (Figure S9). Since the observation of Pt−O interactions is accompanied by the absence of Pt−Nb interactions, we infer that the Pt in the interface of AC-0.4 at 0.1 V_{RHE} predominately interacts with the O in NbO_x rather than the Nb (Figure 5e).

The Pt−O interactions in the Pt−Nb_2O_5 interface were previously conceived by Mitlin et al.[10] based on density functional theory calculations. They further pointed out that the strong Pt−O interactions plus the large geometrical mismatch between the Pt and the Nb_2O_5 force a strong reconstruction of the structure of supported Pt particles. Consequently, the Pt particles are highly distorted and characterized with low CN_{PtPt},[10] and the Pt−Pt bond distance is shortened by the short O−O bond distance in Nb_2O_5. The small and disordered Pt particles in AC-0.4 have been clearly observed by XRD, TEM, and XAS; and the EXAFS analysis further reveals that the R_{PtPt} (2.73 Å) in AC-0.4 is shorter than that of Pt/C (2.75 Å) and Pt/NbO_x/GF systems (Table 1). The remarkable consistency between the experimental and theoretical results firmly verifies the strong Pt−O interactions in the Pt/NbO_x/AC system, which dictates the structural and electronic properties of the supported Pt particles.

It is worth noting that Pt−Nb interactions in AC-0.4 emerge when the potential is increased to 0.54 V_{RHE} as indicated by the CN_{PtNb} of 1.0 ± 0.4 (Figure 5b), which remains unchanged up to 1.1 V_{RHE} (Table 1). Meanwhile, the CN_{PtO} also increases as reflected by the increased intensity of the Pt−O peak around 1.5 Å (Figure 5b), as well as the increased Pt white line intensity (Figure 5d). Given that the CV of AC-0.4 exhibits a typical flat double layer region devoid of OH* adsorption features around 0.54 V_{RHE} (Figure S9), the more pronounced Pt−O interactions observed at 0.54 V_{RHE} cannot be ascribed to the adsorption of oxygen species from water dissociation, which also fails to account for the emerged Pt−Nb interactions. We alternatively propose that the oxygen atoms from the NbO_x penetrate into Pt particles at 0.54 V_{RHE}, grasping the Pt clusters closer to NbO_x (Figure 5f). As a result, a higher fraction of Pt interacts with the oxygen, and some of the Pt atoms become in contact with the Nb located underlying the oxygen layer (Figure 5e and f), which is responsible for the emerged Pt−Nb interactions. This penetration phenomenon is in analogy to the well-known interfacial place-exchange between the adsorbed oxides and the Pt surfaces occurred at elevated potentials.[41,42]

The oxygen adsorption from water dissociation is observed at 1.1 V_{RHE} as reflected by the drastic increase in the Pt−O peak intensity as well as the white line intensity (Figure 5c and d), and also supported by the OH adsorption feature in the CV (Figure S9). Subsequent potential reversal to 0.1 V_{RHE} shows excellent spectral overlap with those collected at 0.1 V_{RHE}

DOI: 10.1021/jacs.7b02378
J. Am. Chem. Soc. 2017, 139, 7893−7903

previously. This indicates a reversible oscillation of the supported Pt particles toward/away from the NbO_x substrate with potentials. These in situ data provide the first evidence for the oscillating nature of MMOI under ORR conditions.

It is noted that the MMOI nature in the Pt/NbO_x/GF and Pt/NbO_x/AC systems is distinctly different. The Pt in Pt/NbO_x/GF mainly interacts with Nb, and consequently the Pt−Nb interactions are observed within the entire potential range from 0.1 to 1.1 V; whereas the Pt−O interactions are only observed at elevated potentials wherein the oxygen comes from O_2 and/or H_2O activation (Table 1). The difference is ascribable to the different oxygen abundance of the MMO interface in the two systems. While the Pt side in the Pt-NbO_x interface is always the metallic Pt, the NbO_x side can be composed of the Nb cations, and/or the O anions depending on the valence state of the NbO_x that determines the oxygen abundance (Scheme 1). The NbO_x side in the interface in AC-0.4 with nearly saturated NbO_x is dominated by O, and thus Pt interacts with O rather than the Nb underlying the oxygen layers until the place-exchange occurs (Scheme 1a). On the other hand, the abundance of oxygen in the interface of the Pt/NbO_x/GF system is largely reduced owing to the unsaturated valence state of Nb, which allows the direct interaction between the Pt and the Nb exposed in the interface (Scheme 1b). These findings point to an intuitive and general picture of MMOI wherein the metal cluster interacts with whatever in the metal oxides located in the MMO interface.

Scheme 1. Interfaces between Pt and the Saturated Nb_2O_5 (a) and between Pt and the Unsaturated NbO_x (b)[a]

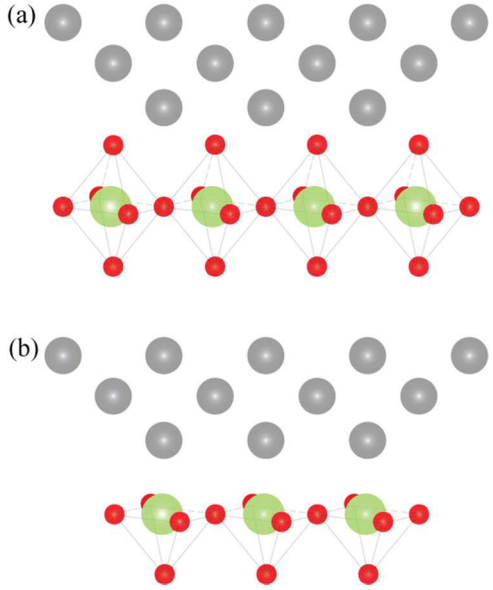

[a]Silver, green, and red balls represent Pt, Nb, and O, respectively.

Electrochemical Characterizations. The profound changes in the structural and electronic properties of the supported Pt particles induced by MMOI exhibits a direct influence in their respective catalytic properties. To verify this, representative Pt/NbO_x/C samples were tested in a RDE to assess their activity and durability toward ORR in acid. The ORR is chosen here considering its high sensitivity to the particle size and electronic properties of Pt particles.[43] As a control, commercial Pt/C (Tanaka Kikinzoku Kogyo, 47%) was also measured under the same conditions as a baseline. As shown in Figure 6a, the electrochemical surface areas (ECSAs) of Pt/NbO_x/AC samples are higher than those of Pt/NbO_x/GF samples, as expected from their smaller particle sizes. The absence of NbO_x overlayers on Pt particles in both Pt/NbO_x/AC and Pt/NbO_x/GF systems is supported by the fact that their ECSAs are comparable or even higher than the counterpart carbon supported Pt clusters with comparable particle size (Figure 6a). Arranging the samples in order of increasing particle size results in a general increase in the specific activity (Figure 6c), and a classic volcano-shape trend of the mass activity (Figure 6b); both follow the activity trends governed by the particle size effect.[43] The superior mass activity of GF-1.6 to that of GF-Pt is ascribed to smaller particles size induced by NbO_x, given that the GF-2.1 with comparable particle size shows comparable specific activity with GF-Pt (Figure 6c). This is in agreement with previous findings that NbO_x offers better overall platinum mass utilization but not higher specific activity.[6] On the other hand, the Pt/NbO_x/AC samples show higher specific activity as well as ECSAs compared to the Pt/C, resulting in marked enhancement in mass activity (Figure 6b). The enhanced specific activity is attributable to the strain effect as indicated by the shortened R_{PtPt}[28,44] and/or the repelling effect induced by NbO_x.[18]

Selected catalysts were subjected to long-term cycling in O_2-saturated 0.1 M $HClO_4$ in a RDE in the potential range of 0.1−1.0 V to investigate the MMOI effects on the durability. This potential region was chosen to minimize the carbon corrosion induced degradation that mainly occurs at higher potentials.[45] As seen in Figure 6d, the durability of Pt/C is significantly improved by NbO_x. Specifically, the Pt/C and GF-Pt possessing only Pt−C interaction (black dashed lines in Figure 6d) are less stable than Pt/NbO_x/GF dominated by Pt−Nb interactions (blue dashed lines in Figure 6d), and the Pt/NbO_x/GF catalysts are less stable than Pt/NbO_x/AC catalysts possessing both Pt−O and Pt−Nb interactions (red dashed lines in Figure 6d). Notably, the particle size of Pt also decreases with the same trend of Pt/GF > Pt/NbO_x/GF > Pt/NbO_x/AC. As a result, the Pt/NbO_x/C systems exhibit an unusual durability trend that generally increases with decreasing particle size. On the contrary, the durability of Pt/C particles increase with increasing particle size since the degradation of Pt/C upon voltage cycling is largely caused by the dissolution of small Pt particles resulting in particle growth via Ostwald ripening and/or agglomeration.[46,47]

The unusual durability trend of the Pt/NbO_x/C system arises essentially from the stabilization of small Pt particles during synthesis as well as long-term operation. This has been observed on Pt/NbO_x and many other MMO systems, and related to the strong MMOI between the Pt and NbO_x that hinders Pt dissolution by tightly anchoring the Pt clusters into the NbO_x support.[4,23,48] This common viewpoint is undermined by a recent finding that small amount of surface-doped metal oxides on the surface of octahedral PtNi/C greatly hinder the dissolution of low-coordinated Pt sites, resulting in the stabilization of the octahedral shape and marked enhancement in ORR durability.[49−51] Therefore, a more general picture can be represented as MMOI stabilizing the low-coordinated sites that are energetically unfavorable and prone to dissolution,[52,53] thereby stabilizing shaped particles and small particles that are characteristically populated with low-coordinated surface sites. The suppression of Pt dissolution by MMOI is supported by the ECSA and the specific activity analysis (Figure S11). While both particle growth and Pt dissolution (note not all the dissolved Pt

DOI: 10.1021/jacs.7b02378
J. Am. Chem. Soc. 2017, 139, 7893−7903

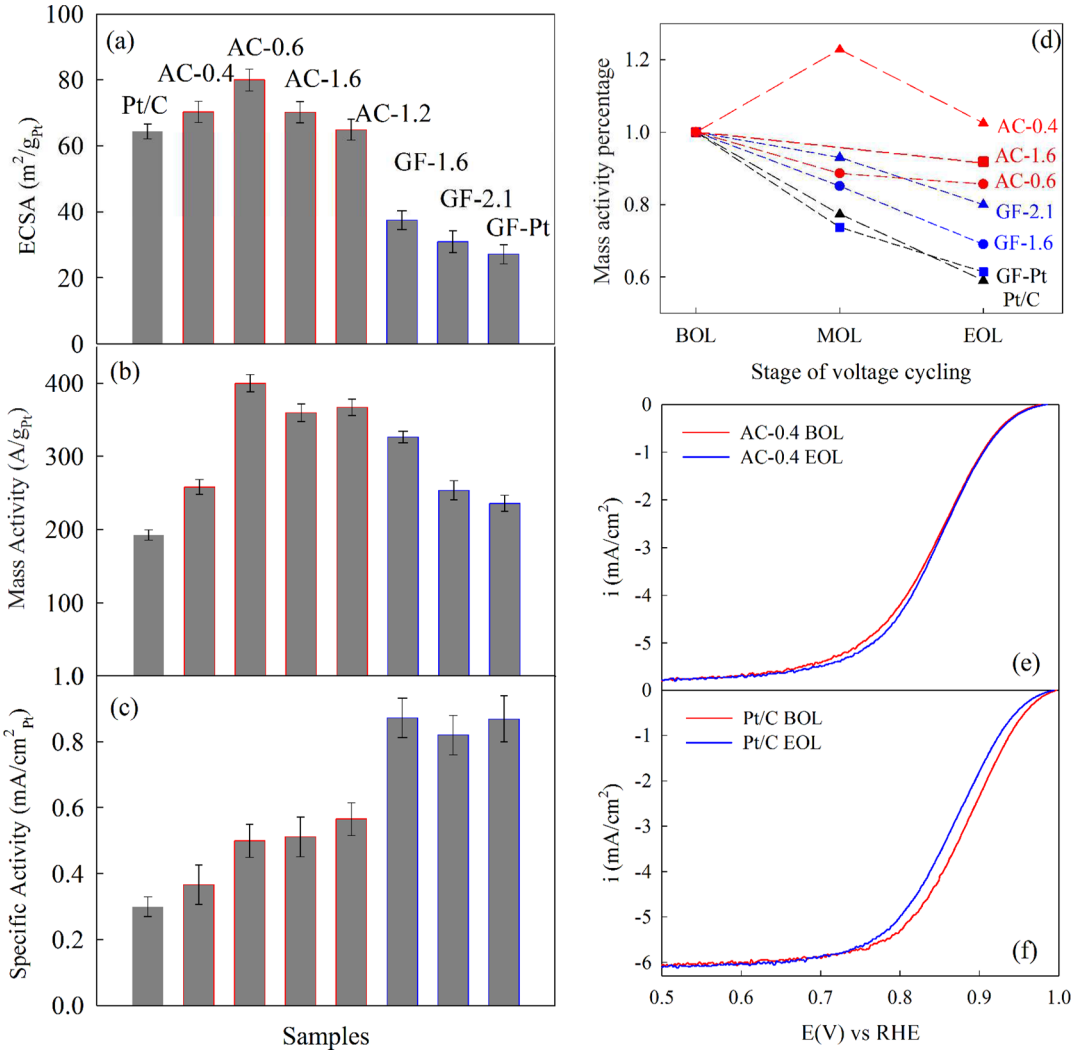

Figure 6. ECSA (a), mass activity (b), and specific activity (c) of indicated catalysts at the BOL stage measured in a RDE in a N_2/O_2-saturated 0.1 M $HClO_4$ electrolyte with a scan rate of 20 $mV{\cdot}s^{-1}$ and a rotation speed of 1600 rpm for ORR polarizations at room temperature; (d) the mass activities of representative catalysts at various cycling stages. ORR polarization curves of AC-0.4 (e) and commercial Pt/C (f) at BOL and EOL stages. The error bars indicate the standard deviations arising from multiple RDE measurements conducted for each catalyst.

will redeposit back onto the electrode) upon voltage cycling cause the ECSA loss (Figure S11a), the former increases the specific activity whereas the latter decreases, and the specific activity change is a counterbalance of these two occurrences. Therefore, the loss, minor changes, and gain in the specific activity of Pt/C, Pt/NbO_x/GF, and Pt/NbO_x/AC (Figure S11b), respectively, upon voltage cycling can be consistently related to the suppression of Pt dissolution by MMOI via the charge transfer from Pt to NbO_x. The stabilization of small particles against dissolution by MMOI is further supported by the post-mortem TEM analysis on the sample AC-0.4 (Figure S12), which shows only mild agglomeration and particle growth upon 25 000 voltage cycles albeit the small particle size.

The central question yet to be answered is how MMOI stabilizes low-coordinated surface sites. It is worth noting that the Pt in the Pt/NbO_x/C system is featured with electron-deficiency owing to the electron flow from Pt to NbO_x. The electron-deficiency increases as Pt/C < Pt/NbO_x/GF< Pt/NbO_x/AC because of the increasing Pt electron donation trend of Pt−C < Pt−Nb < Pt−O. Combining this trend with the particle size trend leads to the observation that the Pt particles with higher electron-deficiency are smaller and more durable. This observation strongly suggests that MMOI stabilizes low-coordinated Pt sites by making them electron-deficient. This argument is supported by the fact that low-coordinated Pt sites have an intrinsic property of electron-deficiency,[19] which drives them to donate electrons to reach a more energetically favorable state when exposed to oxidizing environments such as fuel cell cathodes at elevated potentials via the adsorption of oxygen species.[54,55] The desorption of the oxygenated adsorbates during voltage cycling however resumes these low-coordinated Pt sites back to the energetically unfavorable state and susceptible to dissolution. This mode is in line with previous findings[53,56] that the removal of oxygenated adsorbates destabilizes the low-coordinated Pt sites. Unlike the oxygen adsorbates from O_2 and/or H_2O activation, NbO_x are stable within the entire fuel cell operating potential range in acidic media (Figure S6), and therefore are able to stabilize low coordination Pt sites against voltage cycling by maintaining their electron-deficient state. In addition, the sandwich configuration with the NbO_x stable up to 1.5 V in the middle helps to inhibit carbon corrosion that mainly occurs at high potentials especially in the presence of Pt,[45] but it is beyond the scope of this work.

DOI: 10.1021/jacs.7b02378
J. Am. Chem. Soc. 2017, 139, 7893−7903

DISCUSSION

It has long been recognized that the degree of oxygen incorporation in the MMO interface plays a key role in determining the nature of MMOI, and in turn governs the physical and chemical properties of supported metal particles.[57] This is largely derived from the observation that SMSI can be reversibly activated and deactivated by tuning the valence state of the oxide substrate.[2,5] An appealing explanation for this phenomenon has been conceived wherein the reduction of oxides promotes the exposure of the underlying metal cations by removing oxygen from the interface, hereby allowing for metal−metal interactions.[2,5,7] While this conjecture is intuitive, this work provides direct experimental evidence verifying it by revealing interfacial Pt−Nb interactions for unsaturated NbO_x, and interfacial Pt−O interaction with nearly saturated NbO_x (Scheme 1). This is achieved by the modified APD method that enables systemic modulation of the valence state of the deposited NbO_x under mild conditions. Since the nature of MMOI depends on the oxygen incorporation in the MMO interface, which is very sensitive to many factors such as the valence state of the metal oxides, the structure and composition of the MMO interface, the reductive/oxidative environments, and applied potentials, it is not surprising that various nature of MMOI has been reported across laboratories worldwide.

The supported metal in the MMO interface is electron deficient irrespective of the nature of MMOI, as suggested by the electron flow from Pt to NbO_x for both Pt−Nb and Pt−O interactions. This electron transfer direction is not limited to Pt/NbO_x but applicable to most MMO systems since it is driven by the inherent electron donation tendency from metal to oxygen, and from metal to metal cations with relatively empty d-orbitals.[39] The pronounced electron transfer between metal and metal oxides signifies the strong MMOI.

The strong MMOI can benefit the catalytic applications of MMO systems (Figure 6). It promotes the dispersion of small metal particles, thereby improving precious metal utilization. In addition, the strong MMOI plus the geometrical mismatch between the metal and the metal oxide gives rise to a strong driving force dictating the structural and electronic properties of supported metal particles, which makes it possible to favorably modulate the catalytic properties of supported metal particles. These catalytic consequences of MMOI point to the potentials of MMO systems toward many catalytic applications. For example, the AC-0.6 catalyst exhibits a high Pt mass activity of 0.40 $A \cdot mg_{Pt}^{-1}$ toward ORR, and the activity degrades only 15% after 25 000 voltage cycles (Figure 6). The demonstration that the strong MMOI can benefit both activity and durability of small Pt particles toward ORR is important since small particles are desired for catalytic applications as their high surface-to-volume ratio promotes high utilization of the costly metal.

It is noted that the MMO systems are different from the carbon supported Pt-alloy systems that also exhibit exceptional ORR performance,[58−60] and these two systems are not mutually exclusive. This implicates the possibility of further improvements of ORR catalysts by combining the two systems. The development of Pt-alloy/NbO_x/C system is currently being pursued in our laboratories.

CONCLUSIONS

In this work, we revealed how the Pt interacts with the NbO_x in Pt/NbO_x/C systems under ORR conditions. We showed how the interactions dictate the structural and electronic properties of the supported Pt clusters, and in turn change their ORR performance. The experimental results verify that Pt interacts with the O in the nearly saturated NbO_x, and further interact with the Nb underlying the oxygen layers once the oxygen atoms penetrate into the Pt clusters. On the other hand, Pt interacts mainly with the Nb in the unsaturated NbO_x because the oxygen deficiency leaves some Nb exposed at the interface. These findings indicate that the nature of MMOI is governed by the nature of the MMO interface. That is, the metallic atoms in the metal clusters interact with either the oxygen atoms, and/or metal cations in the metal oxides depending on the composition of the metal oxide in the interface, which is largely dependent on the valence state of the metal oxide. Pronounced electron transfer from Pt to NbO_x was observed in all cases owing to the inherent electron flow tendency from the metal to the oxygen and/or the metal cations. The resultant electron deficiency of Pt in MMO systems stabilizes small Pt particles during synthesis and voltage cycling by stabilizing low-coordinated Pt sites, thereby facilitating the dispersion of small metal particles and ORR durability of MMO systems. In addition, the MMOI together with the geometrical mismatch between the metal and metal oxide strongly force the reconstruction of the structural and electronic properties of the supported metal clusters, which can be utilized to modulate the catalytic properties of MMO systems. Consequently, we demonstrated a Pt/NbO_x/C catalyst with high activity and exceptional durability toward ORR in acid. The nature of MMOI and its correlations to the catalytic properties of MMO systems unraveled here may help future efforts of optimization of MMO catalytic systems through manipulation of MMOI.

ASSOCIATED CONTENT

Supporting Information

The Supporting Information is available free of charge on the ACS Publications website at DOI: 10.1021/jacs.7b02378.

Additional information including sample preparation, XAS and XPS data analysis, and RDE testing results (PDF)

AUTHOR INFORMATION

Corresponding Authors

*zfma@sjtu.edu.cn
*s.mukerjee@neu.edu

ORCID

Qingying Jia: 0000-0002-4005-8894
Jingkun Li: 0000-0003-1699-3089
Sanjeev Mukerjee: 0000-0002-2980-7655

Notes

The authors declare no competing financial interest.

ACKNOWLEDGMENTS

The authors thank Ford Motor Co. for a University Research Program Award, and the National Natural Science Foundation of China (21336003, 21606149). The authors thank Chunchuan Xu, Kerrie Gath, Jun Yang, and James Waldecker from Ford Motor Co. for the work on the sample synthesis, testing, and characterizations, and for the profound discussions on the topic. Use of the synchrotron facilities at the National Synchrotron Light Source, beamlines X19A and X3B at Brookhaven National Laboratory, Upton, NY, is supported by the U.S. Department of Energy, Office of Science, Office of Basic Energy Sciences,

DOI: 10.1021/jacs.7b02378
J. Am. Chem. Soc. 2017, 139, 7893−7903

former under Contract No. DE-AC02-98CH10886. This publication was made possible by the Center for Synchrotron Biosciences grant P30-EB-009998, from the National Institute of Biomedical Imaging and Bioengineering. Supports from beamline personnel Dr. Syed Khalid, Dr. Nebojsa Marinkovic, and Dr. Erik Farquhar are gratefully appreciated. Use of the Stanford Synchrotron Radiation Lightsource, SLAC National Accelerator Laboratory, is supported by the U.S. Department of Energy, Office of Science, Office of Basic Energy Sciences under Contract No. DE-AC02-76SF00515. Use of Beamline 2-2 at SSRL was partially supported by the National Synchrotron Light Source II, Brookhaven National Laboratory, under U.S. Department of Energy Contract No. DE-SC0012704.

REFERENCES

(1) Reich, C.; Kaiser, A.; Irvine, J. *Fuel Cells* **2001**, *1*, 249.
(2) Tauster, S.; Fung, S.; Baker, R.; Horsley, J. *Science* **1981**, *211*, 1121.
(3) Gates, B. *Chem. Rev.* **1995**, *95*, 511.
(4) Yan, L.; Rui, X.; Chen, G.; Xu, W.; Zou, G.; Luo, H. *Nanoscale* **2016**, *8*, 8443.
(5) Tauster, S. J.; Fung, S. C.; Garten, R. L. *J. Am. Chem. Soc.* **1978**, *100*, 170.
(6) Blizanac, B. B.; Pylypenko, S.; Olson, T. S.; Konopka, D.; Atanassov, P. *J. Electrochem. Soc.* **2011**, *158*, B485.
(7) Tauster, S. *Acc. Chem. Res.* **1987**, *20*, 389.
(8) Robba, D.; Ori, D.; Sangalli, P.; Chiarello, G.; Depero, L.; Parmigiani, F. *Surf. Sci.* **1997**, *380*, 311.
(9) Zhang, Z.; Henrich, V. E. *Surf. Sci.* **1992**, *277*, 263.
(10) Zhang, L.; Wang, L.; Holt, C. M.; Navessin, T.; Malek, K.; Eikerling, M. H.; Mitlin, D. *J. Phys. Chem. C* **2010**, *114*, 16463.
(11) Chaug, Y.; Chou, N.; Kim, Y. *J. Vac. Sci. Technol., A* **1987**, *5*, 1288.
(12) Kasowski, R. V.; Ohuchi, F. S.; French, R. H. *Physica B+C* **1988**, *150*, 44.
(13) Johnson, K.; Pepper, S. *J. Appl. Phys.* **1982**, *53*, 6634.
(14) Onishi, H.; Aruga, T.; Egawa, C.; Iwasawa, Y. *Surf. Sci.* **1988**, *199*, 54.
(15) Betta, R. A. D.; Boudart, M. *Proc. 5th lnt. Congress on Catalysis*; Elsevier: North-Holland, Amsterdam, 1972; Vol. 2.
(16) Oh, H.-S.; Nong, H. N.; Reier, T.; Bergmann, A.; Gliech, M.; Ferreira de Araújo, J.; Willinger, E.; Schlögl, R.; Teschner, D.; Strasser, P. *J. Am. Chem. Soc.* **2016**, *138*, 12552.
(17) Frank, M.; Bäumer, M.; Kühnemuth, R.; Freund, H.-J. *J. Phys. Chem. B* **2001**, *105*, 8569.
(18) Sasaki, K.; Zhang, L.; Adzic, R. *Phys. Chem. Chem. Phys.* **2008**, *10*, 159.
(19) Gallezot, P.; Alarcon-Diaz, A.; Dalmon, J.; Renouprez, A.; Imelik, B. *J. Catal.* **1975**, *39*, 334.
(20) Mallmann, A. d.; Barthomeuf, D. In *Studies in Surface Science and Catalysis*; Karge, H. G., Weitkamp, J., Eds.; Elsevier: 1989; Vol. *46*, p 429.
(21) Ponec, V.; Bond, G. C. *Catalysis by metals and alloys*; Elsevier: 1995; Vol. *95*.
(22) Koningsberger, D.; De Graaf, J.; Mojet, B.; Ramaker, D.; Miller. *Appl. Catal., A* **2000**, *191*, 205.
(23) Zhang, L.; Wang, L.; Holt, C. M.; Zahiri, B.; Li, Z.; Malek, K.; Navessin, T.; Eikerling, M. H.; Mitlin, D. *Energy Environ. Sci.* **2012**, *5*, 6156.
(24) Matsubu, J. C.; Zhang, S.; DeRita, L.; Marinkovic, N. S.; Chen, J. G.; Graham, G. W.; Pan, X.; Christopher, P. *Nat. Chem.* **2017**, *9*, 120.
(25) Timperman, L.; Lewera, A.; Vogel, W.; Alonso-Vante, N. *Electrochem. Commun.* **2010**, *12*, 1772.
(26) Meschter, P.; Worrell, W. *Metall. Trans. A* **1976**, *7*, 299.
(27) Arruda, T. M.; Shyam, B.; Lawton, J. S.; Ramaswamy, N.; Budil, D. E.; Ramaker, D. E.; Mukerjee, S. *J. Phys. Chem. C* **2010**, *114*, 1028.
(28) Jia, Q.; Liang, W.; Bates, M. K.; Mani, P.; Lee, W.; Mukerjee, S. *ACS Nano* **2015**, *9*, 387.
(29) Newville, M. *J. Synchrotron Radiat.* **2001**, *8*, 322.
(30) Ravel, B.; Gallagher, K. *Phys. Scr.* **2005**, *2005*, 606.
(31) Newville, M.; Livins, P.; Yacoby, Y.; Rehr, J. J.; Stern, E. A. *Phys. Rev. B: Condens. Matter Mater. Phys.* **1993**, *47*, 14126.
(32) Ankudinov, A. L.; Ravel, B.; Rehr, J. J.; Conradson, S. D. *Phys. Rev. B: Condens. Matter Mater. Phys.* **1998**, *58*, 7565.
(33) Vegard, L. *Eur. Phys. J. A* **1921**, *5*, 17.
(34) Zhang, S.; Plessow, P. N.; Willis, J. J.; Dai, S.; Xu, M.; Graham, G. W.; Cargnello, M.; Abild-Pedersen, F.; Pan, X. *Nano Lett.* **2016**, *16*, 4528.
(35) Mukerjee, S.; McBreen, J. *J. Electroanal. Chem.* **1998**, *448*, 163.
(36) De Graaf, J.; Van Dillen, A.; De Jong, K.; Koningsberger, D. *J. Catal.* **2001**, *203*, 307.
(37) Mukerjee, S.; Srinivasan, S.; Soriaga, M. P.; McBreen, J. *J. Electrochem. Soc.* **1995**, *142*, 1409.
(38) Antonio, M. R.; Song, I.; Yamada, H. *J. Solid State Chem.* **1991**, *93*, 183.
(39) Brewer, L. *Science* **1968**, *161*, 115.
(40) Mavrikakis, M.; Stoltze, P.; Nørskov, J. K. *Catal. Lett.* **2000**, *64*, 101.
(41) Kongkanand, A.; Ziegelbauer, J. M. *J. Phys. Chem. C* **2012**, *116*, 3684.
(42) Alsabet, M.; Grden, M.; Jerkiewicz, G. *J. Electroanal. Chem.* **2006**, *589*, 120.
(43) Shao, M.; Peles, A.; Shoemaker, K. *Nano Lett.* **2011**, *11*, 3714.
(44) Strasser, P.; Koh, S.; Anniyev, T.; Greeley, J.; More, K.; Yu, C.; Liu, Z.; Kaya, S.; Nordlund, D.; Ogasawara, H.; et al. *Nat. Chem.* **2010**, *2*, 454.
(45) Roen, L. M.; Paik, C. H.; Jarvi, T. D. *Electrochem. Solid-State Lett.* **2004**, *7*, A19.
(46) Xu, Z.; Zhang, H.; Zhong, H.; Lu, Q.; Wang, Y.; Su, D. *Appl. Catal., B* **2012**, *111−112*, 264.
(47) Makharia, R.; Kocha, S.; Yu, P.; Sweikart, M. A.; Gu, W.; Wagner, F.; Gasteiger, H. A. *ECS Trans* **2005**, *1*, 3.
(48) Huang, K.; Li, Y.; Yan, L.; Xing, Y. *RSC Adv.* **2014**, *4*, 9701.
(49) Huang, X.; Zhao, Z.; Cao, L.; Chen, Y.; Zhu, E.; Lin, Z.; Li, M.; Yan, A.; Zettl, A.; Wang, Y. M.; et al. *Science* **2015**, *348*, 1230.
(50) Beermann, V.; Gocyla, M.; Willinger, E.; Rudi, S.; Heggen, M.; Dunin-Borkowski, R. E.; Willinger, M.-G.; Strasser, P. *Nano Lett.* **2016**, *16*, 1719.
(51) Cao, L.; Mueller, T. *Nano Lett.* **2016**, *16*, 7748.
(52) Ratke, L.; Voorhees, P. W. *Growth and coarsening: Ostwald ripening in material processing*; Springer Science & Business Media: 2013.
(53) Greeley, J. *Electrochim. Acta* **2010**, *55*, 5545.
(54) Calle-Vallejo, F.; Tymoczko, J.; Colic, V.; Vu, Q. H.; Pohl, M. D.; Morgenstern, K.; Loffreda, D.; Sautet, P.; Schuhmann, W.; Bandarenka, A. S. *Science* **2015**, *350*, 185.
(55) Han, B.; Miranda, C.; Ceder, G. *Phys. Rev. B: Condens. Matter Mater. Phys.* **2008**, *77*, 075410.
(56) Wakisaka, M.; Asizawa, S.; Uchida, H.; Watanabe, M. *Phys. Chem. Chem. Phys.* **2010**, *12*, 4184.
(57) Sanchez, M. G.; Gazquez, J. L. *J. Catal.* **1987**, *104*, 120.
(58) Han, B.; Carlton, C. E.; Kongkanand, A.; Kukreja, R. S.; Theobald, B. R.; Gan, L.; O'Malley, R.; Strasser, P.; Wagner, F. T.; Shao-Horn, Y. *Energy Environ. Sci.* **2015**, *8*, 258.
(59) Jia, Q.; Li, J.; Caldwell, K.; Ramaker, D. E.; Ziegelbauer, J. M.; Kukreja, R. S.; Kongkanand, A.; Mukerjee, S. *ACS Catal.* **2016**, *6*, 928.
(60) Chen, C.; Kang, Y.; Huo, Z.; Zhu, Z.; Huang, W.; Xin, H. L.; Snyder, J. D.; Li, D.; Herron, J. A.; Mavrikakis, M.; et al. *Science* **2014**, *343*, 1339.

DOI: 10.1021/jacs.7b02378
J. Am. Chem. Soc. 2017, 139, 7893−7903